Original Article

Ti6Al4V lattice structures manufactured by electron beam powder bed fusion - Microstructural and mechanical characterization based on advanced in situ techniques

Daniel Kotzem [a,*], Tizian Arold [b], Kevin Bleicher [a], Rajevan Raveendran [a], Thomas Niendorf [b], Frank Walther [a]

[a] TU Dortmund University, Chair of Materials Test Engineering, Baroper Str. 303, 44227 Dortmund, Germany
[b] University of Kassel, Institute of Materials Engineering — Metallic Materials, Moenchebergstr. 3, 34125 Kassel, Germany

ARTICLE INFO

ABSTRACT

Powder bed fusion (PBF) processes enable the manufacturing of complex components in a time- and cost-efficient manner. Especially lattice structures are currently focused since they show varying mechanical properties, including different deformation and damage behaviors, which can be used to locally tailor the mechanical behavior. However, the present process-structure-property relationships are highly complex and have to be understood in detail in order to enable an implementation of PBF manufactured lattice structures in safety-relevant applications. Within the present work Ti6Al4V lattice structures were manufactured by electron beam powder bed fusion of metals (PBF-EB/M). Based on the classification of bending- and stretch-dominated deformation behavior, two different lattice types, i.e. body-centered cubic like (BCC-) and face-centered cubic like (F_2CC_Z) structures were selected. Microstructural features were detected to evaluate if potential different microstructures can occur due to different lattice types and to answer the question if microstructural features might contribute to the mechanical behavior shown in this work. Furthermore, X-ray microfocus computed tomography (μCT) analysis were carried out to enable a comparison between the computer-aided designed (CAD) and as-built geometry. For mechanical characterization, quasi-static and cyclic tests were used. In particular, the BCC lattice type showed a more ductile material behavior whereby higher stiffness and strength was determined for the F_2CC_Z lattice type. Additionally, different in-situ measurement techniques such as direct current potential drop system and digital image correlation could be deployed to describe the damage progress both under quasi-static and cyclic loading.

* Corresponding author.
E-mail address: daniel.kotzem@tu-dortmund.de (D. Kotzem).

1.   Introduction

Since years additive manufacturing (AM) gains much attention due to its characteristic layer-by-layer manufacturing eventually enabling fabrication of components with almost unlimited geometrical design freedom [1,2]. Especially powder bed fusion (PBF) techniques comprising metals such as laser (PBF-LB/M) and electron beam powder bed fusion (PBF-EB/M) are focused since they can be applied to process various metallic alloys, which was already demonstrated in numerous studies [3—7]. Both manufacturing techniques use a high energy source (laser or electron beam) to locally melt powder particles according to a computer-aided designed (CAD) file. However, the PBF-EB/M process offers certain benefits such as higher processing temperatures, which allow to reduce residual stresses, and a vacuum atmosphere, which helps to minimize oxidation processes of oxygen-sensitive materials like Ti alloys [2]. With regard to Ti alloys, the Ti6Al4V alloy is currently the most common representative for Ti alloys capturing nearly half of the worldwide demand for Ti components [3]. In particular, this alloy is known for its good mechanical and corrosion properties as well as its biocompatibility, which is of special interest for biomedical applications [8]. Numerous studies have already been carried out investigating the mechanical behavior of PBF-EB/M manufactured Ti6Al4V bulk material [9—12]. However, as the bulk material in as-built state exhibit a stiffness mismatch ($E_{Ti6Al4V}$ = 118 GPa [13]) compared to the human bone (cortical bone: E = 20 GPa [14]), local stress shielding can occur. Addressing this, different approaches such as the implementation of new material classes as well as patient-optimized designs are currently considered.

Periodic lattice structures are a promising candidate since they can easily be manufactured by AM and enable the local adjustment of material properties by varying the dimensions of the respective lattice type. In literature, the general manufacturability of periodic lattice structures made of Ti-based alloys was already shown [15—19]. Cansizoglu et al. [20] stated that the smallest strut diameter, which can be manufactured by PBF-EB/M without optimizing the process parameters, is 0.7 mm. Based on Ashby [21], the mechanical properties of cellular structures are dependent on the mechanical properties of the base material as well as the topology and relative density of the lattice structure. Furthermore, cellular structures can show either a bending- or a stretch-dominated deformation behavior. The actual type can be quantified by the Maxwell criterion [22]. Typically, bending-dominated structures show good absorption properties, which makes them suitable for energy absorbing applications. Stretch-dominated structures are the preferred choice for lightweight applications due to the increased stiffness and the good mechanical strength, however, they are often characterized by brittle failure of single struts and post-yield softening [21]. Considering the manufacturing process in itself, further variables such as process parameters, process-induced defect distribution and surface roughness have to be considered when determining the mechanical properties of additively manufactured periodic lattice structures. Cheng et al. [15] investigated the deformation behavior under compressive load for stochastic foams and periodic lattice structures fabricated by PBF-EB/M, finally revealing that periodic lattice structures show higher specific strength compared to stochastic foams under similar specific stiffness. Furthermore, several authors [15,23,24] have shown that the results for Young's modulus and compressive strength are almost similar to trabecular and cortical bone. Focusing on recent literature, most researchers investigated the influence of different lattice types [25], different degrees of porosity [26—28] and post heat-treatments [27,29] on the mechanical properties of PBF-EB/M manufactured Ti6Al4V periodic lattice structures. In particular, it was reported that the compressive strength decreases with increasing porosity (lower relative density). Furthermore, it was found by Epasto et al. [27] that actual and CAD geometry show significant discrepancies, which were attributed to the process parameters used. Hernández-Nava et al. [29] investigated the effect of post heat-treatments above and below β-transus temperature on the compressive properties. Thereby, it could be demonstrated that the heat treatment below β-transus temperature has a negligible effect. Furthermore, the as-built condition was found to be similar to an annealed condition. A heat-treatment above β-transus promoted the evolution of a coarser microstructure and a decrease in the compressive strength. This was confirmed by Galati et al. [30]. Since it was stated that the as-built surface roughness also plays an important role for periodic lattice structures, Formanoir et al. [31] used chemical etching in order to improve the surface quality of Ti-based lattice structures. Compared to the as-built state, an increased relative stiffness could be determined.

As can be deduced from the previous section, most studies focused on the determination of the deformation behavior under compressive load. Focusing on the cyclic material properties of PBF-EB/M manufactured Ti6Al4V, only scarce data are currently available. Li et al. [32] investigated the compression fatigue behavior of PBF-EB/M manufactured Ti6Al4V lattice structures. Specimens with different degrees of porosity were manufactured and it could be elaborated that fatigue strength increases with decreasing porosity following the Gibson-Ashby model [33]. Furthermore, the influence of different cell morphologies on the compression fatigue behavior was analyzed by Zhao et al. [34]. In a more recent study, Lietaert et al. [35] investigated the fatigue behavior of PBF-EB/M manufactured Ti6Al4V lattice structures under various fatigue regimes (tension-tension, compression-compression, tension-compression). It was reported that the compression-compression and tension-tension fatigue regime promote an inferior fatigue life compared to the fully-reversed loading. Such behavior was attributed to the local mean stress. Furthermore, fracture sites were found to be located close to the nodes, where highest tensile stresses are located. However, from literature [9,15,31,34] it is evident that several factors such as process parameters, surface quality, lattice morphology and post-processing can influence the mechanical properties of PBF-EB/M manufactured Ti6Al4V lattice structures which make a general comparison with other studies quite challenging. Further on, the deformation and damage behavior of bending- and stretch-dominated lattice structures are yet not fully understood and further studies are needed to enable more potential application fields

for AM lattice structures. One major objective to address this issue might be the implementation of in-situ measurement techniques in order to clearly describe the damage progress especially under cyclic loading. In prior investigations, the authors already investigated the deformation and damage behavior of small-scale struts [36] as well as within a single unit-cell plane [37] by using various measurement techniques such as acoustic emission analysis, temperature and resistance measurements as well as digital image correlation (DIC) in order to monitor the damage progress under cyclic loading. Thereby, particular material reactions could be clearly correlated with the measurement quantities recorded. As a consequent step forward, these measurement techniques should now be adapted towards complex lattice structures consisting of several linked unit-cells, whereby appearing challenges are highlighted and compared with known literature. Within this work, the microstructural and mechanical properties of PBF-EB/M manufactured Ti6Al4V lattice structures in as-built state are investigated. As a basis for in-depth evaluation, microstructural investigations using scanning electron microscopy (SEM) and hardness mappings are considered. For mechanical characterization, a novel approach for calculating the nominal cross section of lattice structures is introduced in order to create a basis for a reliable comparison with existing data from literature. Quasi-static and cyclic tests are conducted for characteristic bending-dominated body-centered cubic like (BCC) and stretch-dominated face-centered cubic like (F_2CC_Z) lattice types, whereby measurement methods such as the direct current potential drop (DCPD) technique and DIC are used in order to detect upcoming material reactions which can straightforward be correlated with the increasing damage progress.

2. Experimental procedure

2.1. Materials and manufacturing techniques

For manufacturing of the specimens an Arcam A2X (GE, Sweden, Mölndal) equipped with the software EBMControl version 4.201 was used. The Ti–6Al–4V powder with the powder particle size distribution ranging from 45 to 105 μm was supplied by the machine vendor Arcam. The process parameter for Ti–6Al–4V as recommend by Arcam were used. Since "Automatic Power Calculation" is activated in the recommend process parameter settings. Due to this specific parameter setting the speed and current of the beam are adapted to the scan path length, which especially for lattice structures does change over build height. Both lattice type specimens, BCC and F_2CC_Z were placed on one 150×150 mm^2 AISI 304 start plate. All specimens were manufactured upright, i.e. parallel to building direction. The initial strut diameter was set to 1 mm for both lattice types and the unit cell size was $7 \times 7 \times 7$ mm^3. This leads to a relative density of 0.0968 for the BCC and 0.0908 for the F_2CC_Z specimen, respectively. In total, $3 \times 3 \times 3$-unit cells form the lattice structure for tensile and fatigue testing and $5 \times 5 \times 5$-unit cells for compression testing. The processing time was about 14 h, followed by a cooling phase of about 6 h (cf. Fig. 1). The temperature was measured by means of a thermocouple attached
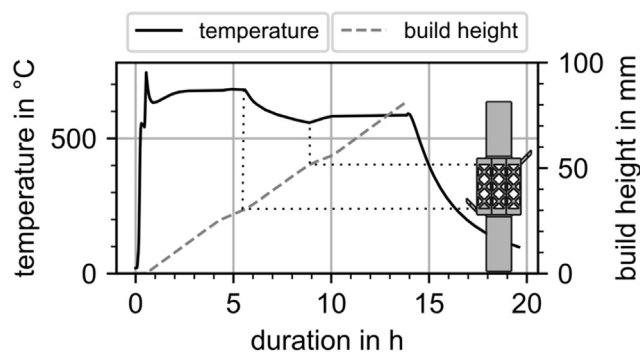

Fig. 1 – **Process temperatures and build height over processing time.**

to the bottom of the start plate. During the processing of the lattices the processing temperatures dropped from 680 down to 560 °C due to a significantly reduced sample cross section and, hence, a reduced energy input. Thereafter, the initial temperature was not reached again due to geometrical reasons, i.e., an increased distance between the uppermost layer and the platform as well as limited heat flux across the lattice structure.

2.2. Microstructural investigations

The F_2CC_Z and BCC specimens were wire cut by electric discharge machining as detailed in Fig. 2 to allow for microstructure analysis. The specimens were ground using abrasive paper to P4000, followed by manual diamond polishing with 3 and 1 μm diamond suspension and subsequent vibro-polishing for 4 h with the colloidal silica suspension Master-Met 2. For both specimen types electron backscatter diffraction (EBSD) measurements were carried out at a build height of 51 and 44 mm, respectively, at the nodes of two unit cells.
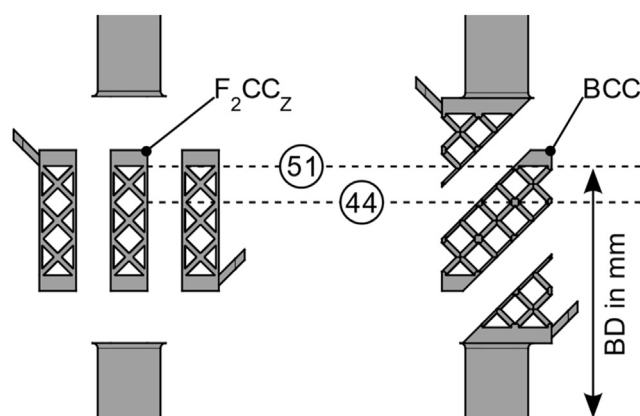

Fig. 2 – **Schematic representation of the specimens cut for microstructure and hardness testing from the F_2CC_Z and BCC lattices. The dotted lines represent the build height, measured from the base plate, at which microstructural investigations and hardness measurements were carried out.**

Grain morphology and phase composition were characterized using a Zeiss Ultra Plus scanning electron microscope equipped with an EDAX EBSD detector. The investigated surface areas per node were about 4900 μm^2 with a spatial resolution of 0.1 μm per pixel. The EBSD data were investigated by using TLS OIM Software. Grains were defined based on an orientation deviation of at least 15°. Since the α-phase in Ti6Al4V does appear in a lamellar fashion, the α-laths width can be deduced from the minimum feret diameter. To investigate if the specific geometry of the lattice structure does have an influence on the final thermal gradient, the minimal feret diameters deduced from each EBSD measurement were compared to each other. Here, it is assumed that the heat flux across a lattice structure is strongly hampered compared to bulk material. A hampered heat flux can be linked to much slower cooling of the melt and, eventually, to an increase of the α-lamella width. To compare the data with each other a statical approach was chosen. As the Levene test revealed inconsistent variances in feret diameter, the Kruskal-Wallis test was conducted to answer the question, if there are significant differences in terms of the mean minimum feret diameter in case of different lattice types and at different build heights, respectively. To reveal which conditions do differ from each other, the post-hoc pairwise multiple comparison Conover test was conducted. The Benferroni-Holm p-value correction, which is the most stringed correction function and offers the least probability for difference detection, was used to ensure that the data are not misinterpreted.

2.3. Hardness

For hardness measurements a DuraScan 70 (Struers, Willich, Germany) was used. Hardness was measurement in the nodes of the unit-cells of the BCC and F_2CC_Z specimens (embedded in resin) at build heights of 51, 44 and 37 mm, respectively. For each build height 10 measurement points were considered in one single node. Because of the limited space within the struts and nodes, the testing forces for single measurements as well as the hardness mapping were chosen as 0.98 N. Thus, a relatively high number of measurement points could be placed without violating the required minimum distances, i.e., 3 times the length of the indent diagonal between single indents. Hardness mappings, spanning an area of 2.4 mm times 0.6 mm, were collected at a build height of 44 mm, starting within a strut close to the node of the unit-cells.

2.4. Micro computed tomography

To determine the nominal cross section of the PBF-EB/M manufactured lattice structures, X-ray microfocus computed tomography (μCT) was carried out. The system XT-H 160 (Nikon Metrology, Tokyo, Japan) was used, which is characterized by a maximum acceleration voltage of 160 kV and a micro-focus of 3 μm. The corresponding scanning parameters
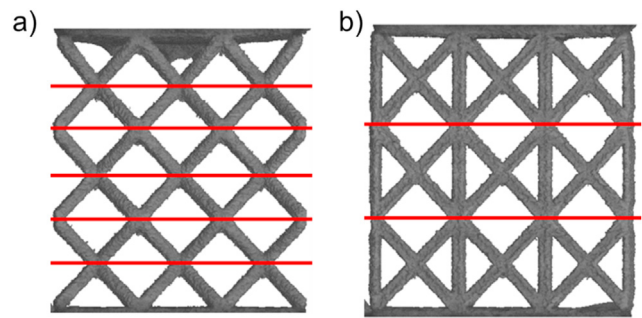

Fig. 3 − Schematic representation of the cutting planes for the determination of the nominal cross section for a) the BCC and b) the F_2CC_Z lattice type.

are listed in Table 1. Depending on the specimen size, different effective pixel sizes were realized.

Based on the reconstructed volumes, two-dimensional slices at positions with minimal cross section, exemplary highlighted for a tensile/fatigue specimen in Fig. 3a−b, were determined and imported into the software ImageJ. Afterwards, every slice was scaled and converted into a black/white image (binarization) based on a defined threshold value. Then, the nominal cross section was calculated and averaged for every investigated specimen. The consecutive steps for the cross section-determination are highlighted in Fig. 4a−c. The cross section for the compression specimens ($5 \times 5 \times 5$-unit cells) was calculated analogously. In order to provide a sufficient number of sectional images, at least three specimens were considered for every lattice type.

2.5. Mechanical testing

As already mentioned, specimens with different lattice types (BCC and F_2CC_Z) were investigated. In terms of mechanical characterization, quasi-static as well as cyclic tests were carried out. For the quasi-static compression and tensile tests, the servohydraulic system Schenck PSB 100 with Instron 8800 controller was used, which is equipped with a 75 kN load cell. Both tests were conducted under constant crosshead displacement ($v_{c,comp.} = 1$ mm/min, $v_{c,ten.} = 1.5$ mm/min). Strains were determined by contactless digital image correlation (DIC), whereby an Imager M-Lite camera (LaVision, Goettingen, Germany) was used. Before, specimens were colored black and a fine white speckle-pattern was applied. To characterize the fatigue properties, a combination of multiple step (MST) and constant amplitude tests (CAT) was conducted. A servohydraulic system Schenck PC63 M with Instron 8800 controller was used being equipped with a 45 kN load cell. All experiments were carried out with a test frequency of f = 3 Hz and the load ratio was set to R = −1 (tension-compression).

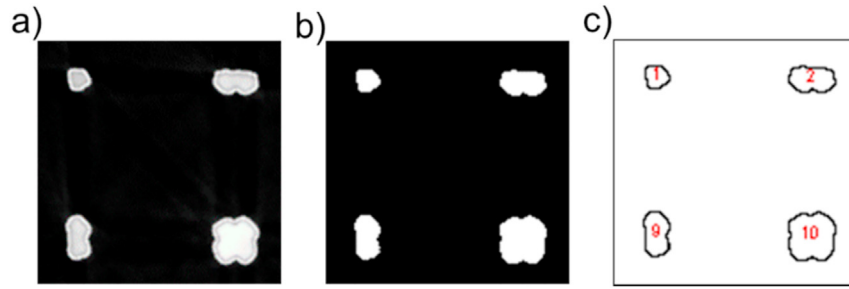| Table 1 − Scanning parameters for computed tomography scans (μCT).						
Material	Beam energy	Beam current	Power	Effective pixel size	Exposure rate	
Ti6Al4V	150 kV	62 μA	9.3 W	30−55 μm	354 ms	2.82 fps

Fig. 4 — Image processing steps to calculate the nominal cross section; a) original image, b) binarization and c) derived data.

During the MST, the initial load was set to $\sigma_a = 5$ MPa and was increased stepwise by 5 MPa after every 10^4 cycles. Related material responses were captured by means of different measurement techniques consisting of a direct current potential drop (DCPD) measurement system (Ametek, Berwyn, PA, USA) and a DIC system, the latter being similar to the one used for quasi-static testing. The experimental setup is highlighted in Fig. 5a and b. Since huge amount of data can be generated during such advanced cyclic tests, a triggered image acquisition was applied. Related details were already introduced in Ref. [37]. Based on the results obtained, values for total maximum strain ($\varepsilon_{a,t}$) as well as dynamic Young's modulus (E_{dyn}) were calculated, whereby E_{dyn} was approximated as linear slope between the two reversal points of the hysteresis. After cyclic testing, selected specimens were chosen for fractographic analysis using an SEM Mira 3 XMU (TESCAN, Brno, Czech Republic).

3. Results and discussion

3.1. Microstructure

Inverse pole figure (IPF) maps in Fig. 6 show a basket weave α-lath microstructure for both lattice types and all build heights. This kind of microstructure is often reported in PBF-EB/M processed Ti6Al4V [38,39]. Since the α-lath widths is depending strongly on thermal conditions during processing [40], it can be used to assess if the build height and lattice type do have an effect on the microstructure of PBF-EB/M processed Ti6Al4V. Downing et al. [41] showed that, in general, the nominal temperature within a lattice structure is increasing over the build height and that BCC lattices accumulate more heat over build height than F_2CC_Z lattices.

As shown in Fig. 7, the α-lath width for the BCC specimen increases over 7 mm build height, i.e., the height of a unit cell from 0.625 to 0.725 μm, which might be a direct result of a higher heat accumulation in BCC lattice structures. Since the 95% ci intervals of the F_2CC_Z specimen are overlapping the α-lath width reduction over build hight for F_2CC_Z lattice might just result from data variability.

Furthermore, the results obtained by application of the Conover test (Table 2) do confirm statistically significant differences in α-lath width between BCC and F_2CC_Z in general as well as an increase of α-lath widths over build height for the BCC lattice (but not for F_2CC_Z). These findings are in good agreement with the more pronounced temperature accumulation over build height for BCC lattices revealed by Downing et al. [41]. Most literature found for PBF-EB/M processing of Ti6Al4V does report an α-lath width about 1.5 μm for processing temperatures close to 700 °C [42,43]. Fig. 1 revealed that during processing of the lattice sections, however, the
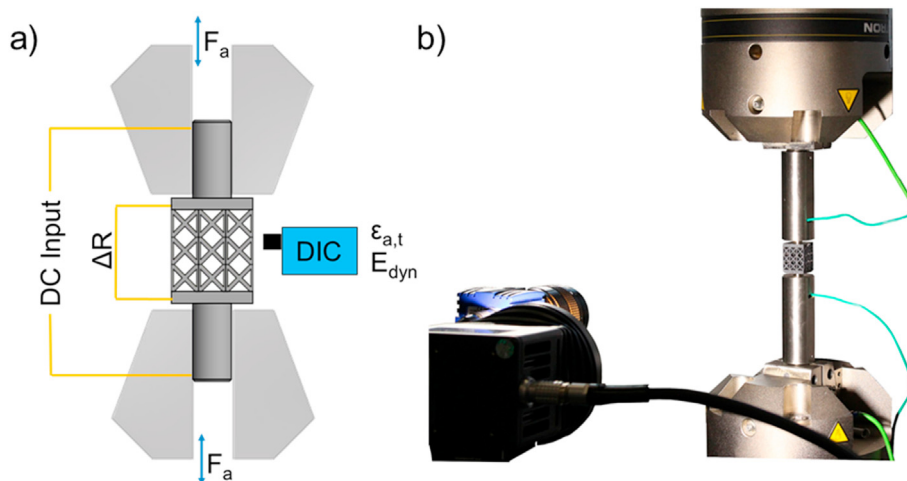

Fig. 5 — a) Schematic illustration and b) photograph of the experimental setup used for cyclic testing.
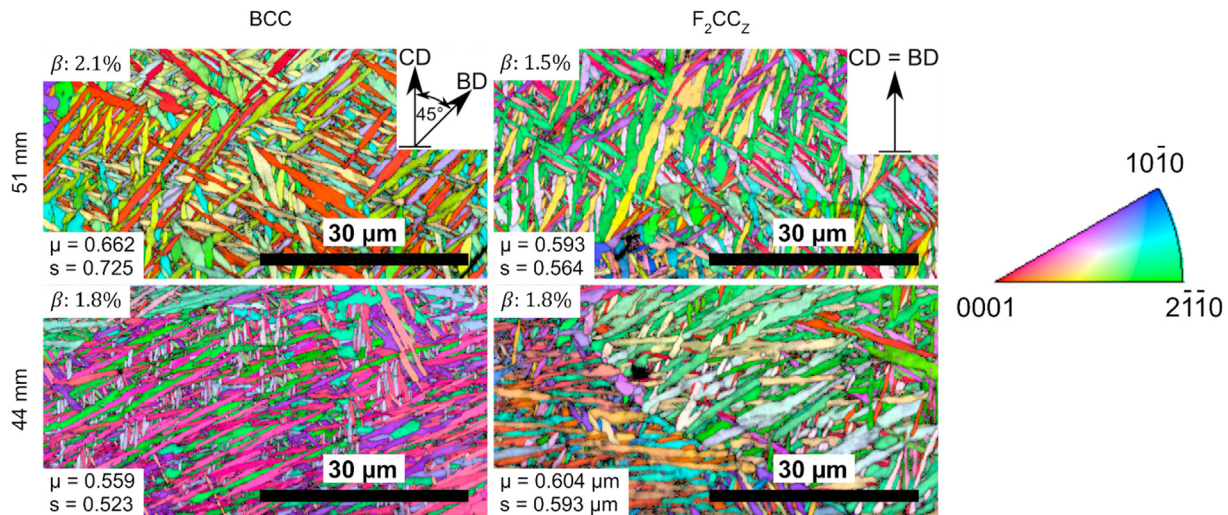
Fig. 6 − **Grain orientation maps obtained by EBSD for the BCC and F_2CC_Z lattice specimens at a build height of 51 and 44 mm, respectively. The arithmetic mean (μ) and the standard deviation (s), both in μm, for the minimum feret diameter for each EBSD measurement are plotted in the lower left corner of the corresponding image. The upper left corner of each image shows the volume fraction of the remaining beta phase. The colour key is induced for the cutting direction (CD). The alignment of CD regarding the build direction (BD) is shown in the upper right insets of BCC and F_2CC_Z at a build height of 51 mm.**

process temperatures dropped from 680 down to 560 °C, this fact being rationalized by a reduction of the overall energy input. Here, the decreased process temperature is thought to be the reason for faster cooling and, hence, smaller α-laths widths than usually reported for bulk material.

3.2. Hardness

The BCC specimen used for hardness measurements was extracted from the original BCC lattice oriented at an angle of 45° to the build direction (cf. Fig. 2). Chang et al. [44] showed that the orientation of a specimen taken from the processed Ti6Al4V material with respect to the build direction does not
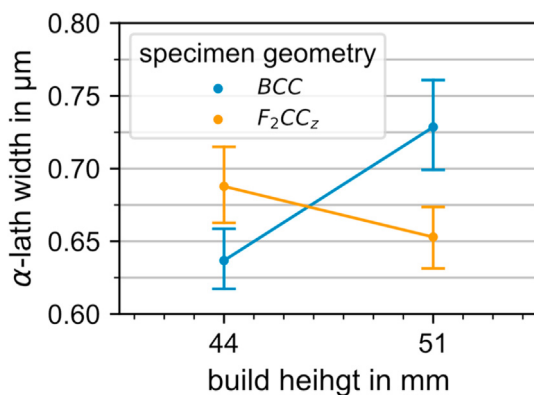
affect the hardness. Due to the anisotropic hardness behavior, the cutting plane orientation influence on hardness should be neglectable. Thus, despite the hardness maps do cover the same strut length of about 2 mm, the BCC specimen does only cover a distance of about 1.4 mm with respect to the build height, while the F_2CC_Z covers 2 mm. Anyhow, the maps shown in Fig. 8 do not reveal any traces of pronounced heterogeneity in terms of mean hardness or standard deviation.

Fig. 9 shows the development of the hardness for the BCC and F_2CC_Z lattices over the build height. A decrease in hardness from 346 ± 17 to 328 ± 32 HV over 14 mm build height can be deduced. Considering the standard deviation of the single sets of hardness measurements for BCC and F_2CC_Z lattices, it is important to point out, that from a statistically point of view no trend can be seen. However, especially for the BCC specimen the mean hardness over the build height is decreasing, which is in good agreement with the higher heat accumulation in BCC lattices predicted by done by Downing et al. [41] and hence the increase in α-lath width shown in Fig. 7. For the F_2CC_Z lattice no clear trend in evolution of hardness over build

Fig. 7 − **α-lath width represented by the minimum feret diameter over build height for the BCC and F_2CC_Z lattices obtained from the grain files calculated with the TLS OIM software. The error bars represent the 95% ci interval.**

Table 2 − **Results of the post-hoc Conover test for multiple comparison of the mean minimum feret diameter of each EBSD measurement applying Benferroni-Holm p-value correction.**

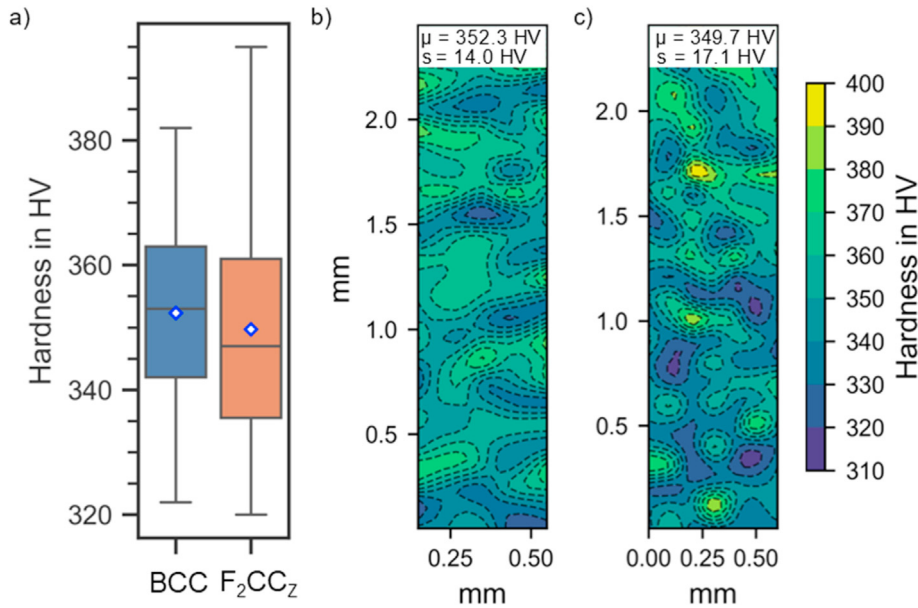|	BCC 44	BCC 51	F_2CC_Z 44	F_2CC_Z 51
BCC 44	1	<1*10^{-6}	0.046166	0.000114
BCC 51	<1*10^{-6}	1	<1*10^{-6}	0.000400
F_2CC_Z 44	0.046166	<1*10^{-6}	1	0.079223
F_2CC_Z 51	0.000114	0.000400	0.079223	1

Fig. 8 – Hardness values extracted from the mappings conducted at a build height of 44 mm for the BCC and F$_2$CC$_Z$ lattices depicted as box plot in a) and corresponding maps for the BCC lattice in b) and the F$_2$CC$_Z$ lattice in c). The mean hardness and standard deviation for each lattice type can be found to the top of each corresponding map.

height can be seen as neither a development of the α-lath width over build height from the data. This can be explained by the predicted minor heat accumulation in this lattice type and, hence, a less pronounced increase of the width of the α-laths. Due to the specimen design, as well as the needed cutting plane orientation of 45° for the BCC specimen, hardness values are only comparable over a build height ranging from 37 up to 51 mm. Measuring hardness at any other location outside of the lattice structure might lead to false conclusions about the influence of the unit cell design and total

Fig. 9 – Values obtained by Vickers hardness tests for the BCC and F2CCZ lattices for build heights of 51, 44 and 37 mm. The grey vertical lines inside of the boxes represent the calculated median while the blue-white squares represent the arithmetic mean and the grey diamonds outliers.

lattice dimension on the microstructural and hardness development. The investigation of higher build heights, i. e. a higher number of linked unit cells was not scope of this work. Looking at the results depicted, and due to the only minor increase of the α-lath width over build height, as well as only minor differences between BCC and F$_2$CC$_Z$ lattices, it is expected that the local microstructure does not alter the mechanical tests in a quantifiable way. However, it must be considered that larger BCC lattice structures, might lead to more distinct differences in α-lath width over build height and hence to local build height dependent mechanical properties. Syed et al. [45] showed that in PBF-EB/M processing the build height and its influence on α-lath width impacts the fatigue behavior of Ti6Al4V processed parts. An increase in α-lath width from 0.9 to 1.1 μm in processed bulk material over a build height of 90 mm reduced the maximum stress amplitude about 2% while the plastic strain range is increased about 60%. Furthermore, the data of Syed et al. [42] showed an increase of α-lath width from 0.9 ± 0.45 to 1.0 ± 0.43 μm over a build height of 50 mm. In the present study, the α-lath width increases from 0.49 ± 0.52 to 0.54 ± 0.73 μm within 7 mm of build height. Hence, build height dependent local mechanical properties might become quantifiable for an increased number of linked unit cells, which exceed the relative build height of 21 mm used in this study. Furthermore, it cannot be excluded that different unit cell types and lattice dimensions impact the local melting and solidification behavior, which might contribute to the differences in hardness and α-lath width between the different lattice types. A more detailed investigation of the size-dependent microstructural development of lattice structures would greatly profit from simulations and will be scope of future work.
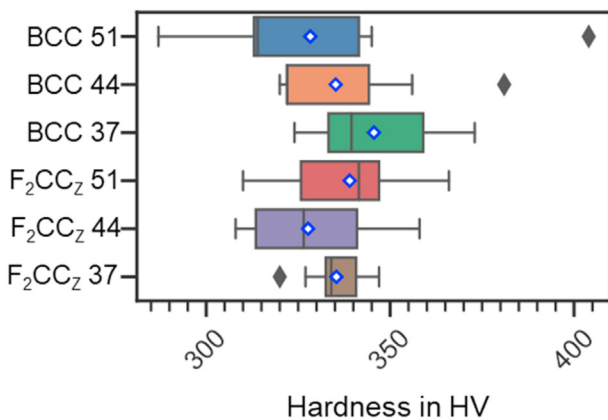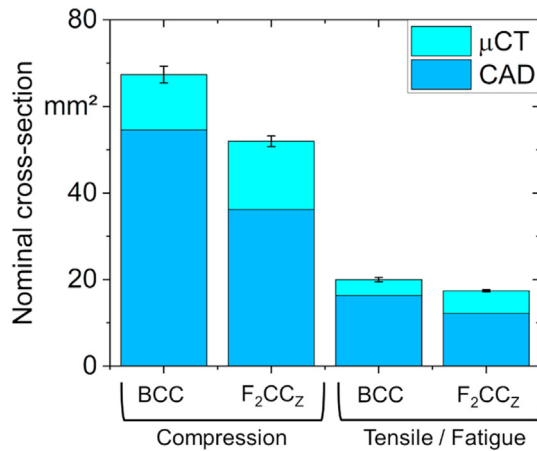
Fig. 10 − Comparison between CAD and μCT cross section dimensions for compression and tensile/fatigue specimens.

3.3. Defining relevant cross-sections of PBF-EB/M as-built lattice structures

As already stated in numerous studies, i.e. in Refs. [46,47], additively manufactured components can be characterized by geometrical deviations, which can complicate the design and construction process. To determine the nominal cross section of the lattice structures used, especially for the later mechanical tests, μCT scans were carried out for every lattice type, whereby at least three specimens were probed, respectively. Details on the approach followed are highlighted in section 2.4.

The reason for considering the nominal cross section based on the μCT scans was given by Suard et al. [48] showing good results in terms of stiffness prediction for calculated equivalent diameters based on μCT scans instead of considering the CAD or geometrical equivalent (inscribed cylinder) diameter. The CAD cross section as well as the real cross section, which was calculated based on the μCT scans, are plotted in Fig. 10 for both lattice types. Furthermore, absolute values are listed in Table 3.

Direct comparison of the results reveals significant deviations. For details on the sections probed see Figs. 3 and 4. All real specimen dimensions are characterized by a larger cross section when compared to the initial CAD data. In detail, the BCC-specimens (compression and tensile/fatigue) show a maximum deviation of around 23%, whereby higher deviations, in total 43%, were determined for F_2CC_Z-specimens. In contrast, it was reported in Ref. [48] that as-manufactured

struts are generally smaller than prescribed by the CAD data. Arabnejad et al. [47] have stated that geometrical deviations of single struts are dependent on the angle towards the building plane. More specific, highest deviations were found for overhanging horizontal struts, which can be attributed to the differences in heat flux between the solid strut and the surrounding powder-bed. Furthermore, partially melted powder particles were observed on the down-facing side leading to an increased surface roughness [48] and a changing strut morphology from circular to elliptical [47]. Another explanation for an increased strut thickness was given by van Bael et al. [29] showing that an increased strut thickness and surface irregularities can result from the staircase effect, this effect being well-known in AM parts. Additionally, it was highlighted in Refs. [26,47] that geometrical deviations between the CAD dimensions and as-built specimens can arise from powder particles that get stuck within pores or corners provoking material agglomerations. These could even explain the positive deviations, which were observed during the determination of the nominal cross sections of the BCC- and F_2CC_Z-specimens (cf. Fig. 10). However, geometrical deviations were found to be in the same range for similar lattice types, i.e., independent of the number of unit-cells. This underlines the high reproducibility of the PBF-EB/M process itself, which was already concluded in Ref. [26]. For mechanical characterization only the cross sections, which were calculated based on the μCT scans, are considered. Nevertheless, it has to be emphasized already at this point that potential mismatches in the geometrical appearance should be considered for the later design process [49]. Sombatmai et al. [50] stated that the effect of geometrical inaccuracies, i.e., undersizing or oversizing of single struts, both are the main reasons for a possible discrepancy between experimental results and numerical simulations. To prevent this, Chahid et al. [51] recently proposed a method to design a lattice CAD model with a designed surface texture which is more representative for the as-built condition.

3.4. Quasi-static properties

3.4.1. Compression properties
The stress-compression curves obtained from the quasi-static compression tests for representative BCC- and F_2CC_Z-specimens are depicted in Fig. 11. In line with DIN 50106 [52], compressive strength $\sigma_{c,p,0.2}$ was determined at 0.2% plastic deformation. For the BCC-specimen, a compressive strength of $\sigma_{c,p,0.2}$ = 71.1 MPa was found. A significantly higher $\sigma_{c,p,0.2}$ = 367.3 MPa was found for the F_2CC_Z-specimen. Clearly, the BCC-specimen shows a more ductile deformation behavior. Within the quasi-static compression tests, several stages with characteristic material responses can be identified for both

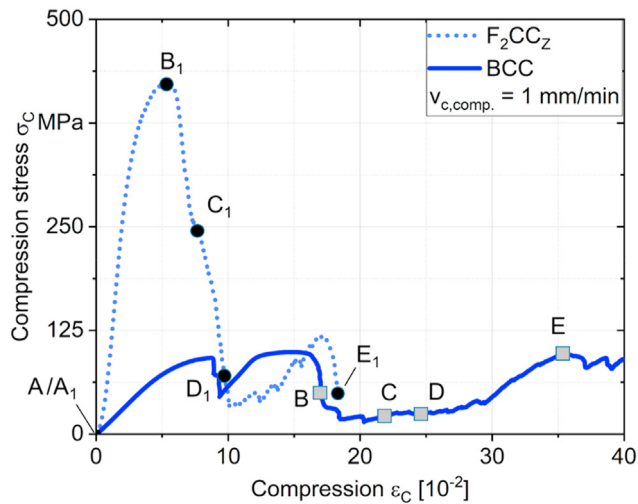| Table 3 − Calculated nominal cross sections for compression and tensile/fatigue specimens based on CAD and μCT data.				
Specimen type	Lattice type			
	BCC (CAD)	BCC (μCT)	F_2CC_Z (CAD)	F_2CC_Z (μCT)
Compression	54.58 mm²	67.38 ± 1.94 mm²	36.19 mm²	51.97 ± 1.22 mm²
Tensile/Fatigue	16.31 mm²	20.01 ± 0.50 mm²	12.17 mm²	17.41 ± 0.25 mm²

Fig. 11 — Stress-strain response obtained by quasi-static compression tests on representative BCC- and F_2CC_Z-specimens. Points labelled by letters refer to the DIC images shown in Fig. 12.

lattice types. For the BCC-specimen, these are referred to as A-E, for the F_2CC_Z-specimen as A_1-E_1, respectively. The corresponding DIC images at these stages can be found in Fig. 12.

In general, two different failure mechanisms are found in case of the investigated lattice types. At stage A/A_1 both specimens are shown in unloaded condition (cf. Fig. 12). In case of the BCC-specimen, thereafter a collapse of cells in planes perpendicular to the load direction is seen. Such behavior could be observed for several cell planes, whereby numerously strength first dropped and then recovered to the same load level being present before. At stages B-E, the consecutive steps of failure are highlighted. Specifically, a given cell plane collapses under the prevailing compression load, eventually leading to a sudden load drop. As a consequence, struts in the next cell plane are subjected to a bending load, which can be clearly seen at stages C and D (cf. Fig. 12). Finally, a densification (stage E) takes place and the cell plane in focus is compressed into the next one. In consequence, the previous steps are repeated. In case of the F_2CC_Z-specimen a different material behavior can be seen. As already mentioned, a significantly higher $\sigma_{c,p,0.2}$ could be determined, however, a more brittle material behavior is found compared to the BCC-specimen. At stage B_1, a peak load position can be seen. Here, certain outer struts already show buckling and stress concentrations can be found in the struts oriented parallel to the loading direction. After reaching the peak stress, first failure occurred, which is highlighted within stage C_1 and D_1 (cf. Fig. 12). It can be seen that oblique oriented struts suffered a diagonal shear load. After this, a densification takes place leading to nearly 32% of the initial peak load until the next partial failure occurred.

3.4.2. Tensile properties
In Fig. 13 the stress-strain curves for representative BCC- and F_2CC_Z-specimens are shown. Similar to the compression curves, the F_2CC_Z-specimen is characterized by higher

mechanical strength directly compared to the BCC-specimen. A yield strength of $\sigma_{YS,F2CCZ} = 373.9$ MPa was determined for the F_2CC_Z-specimen and $\sigma_{YS,BCC} = 155.7$ MPa for the BCC-specimen. Again, several stages with specific material responses within the test could be detected for both lattice types and the corresponding DIC images for stages A-E (BCC-specimen) and A_1-E_1 (F_2CC_Z-specimen) are plotted in Fig. 14. At stage A/A_1 specimens are shown in unloaded condition. Focusing on the Young's modulus of both lattice types, it can be seen that the F_2CC_Z-specimen exhibits a higher stiffness ($E_{F2CCZ} = 34$ GPa) in direct comparison to the BCC-specimen ($E_{BCC} = 6.5$ GPa). Considering the course of the stress-strain curve, it can be deduced that the BCC-specimen can bear again 93% of the initial peak load after the first (stage C) and 85% after the second load drop (both drops corresponding to local failure within the structure). Furthermore, a high degree of deformation is clearly visible at point E revealing a fairly ductile material behavior with a fracture strain $\varepsilon_f = 17.9\%$ for the BCC lattice. On the contrary, the F_2CC_Z-specimen is characterized by a more brittle behavior, since fracture strain was found to be relatively low ($\varepsilon_f = 8.7\%$). Furthermore, the load drop after reaching stage B_1 was found to be more significant and the specimen could bear again only 63% of the initial peak load. First failure was initiated within the transition area to the bulk material, however, final failure occurred on a 45° plane (with respect to loading direction) which could not be captured by DIC, as only one plane of view was monitored.

Lattice structures are generally defined as structures that can be produced based on the repetition of unit-cells with a defined geometry throughout the three-dimensional (3D) space [53]. In an early study [15], it was demonstrated that periodic lattice structures show higher specific strength compared to stochastic foams with similar specific stiffness. This was attributed to the periodic symmetry of these structures, which can easily be defined by a small number of design parameters [54]. In particular, the base material, the cell morphology and the relative density were found to prescribe the mechanical properties of the lattice structures [21].

According to Nazir et al. [55] 90% of metallic cellular materials have yet been fabricated using PBF processes, however, only a small number of industrial applications using AM lattice structures can currently be found due to concerns regarding their structural integrity. In order to address more future application fields, numerous studies were already carried out investigating influencing parameters such as different materials [56,57], lattice types [58] and heat-treatments [29] on the quasi-static deformation behavior. A general classification for lattice structures into bending- and stretch-dominated types can be done based on the Maxwell criterion [22], which provides important information about the mechanical behavior. Stretch-dominated structures are typically more efficient and favored for lightweight constructions since struts are loaded almost exclusively in tension or compression. The stress-response of stretch-dominated lattice structures in compression is typically characterized by higher initial stiffness and higher compressive strength compared to bending-dominated structures with similar relative density [54]. Considering the results presented, the distinction between a bending- and stretch-dominated
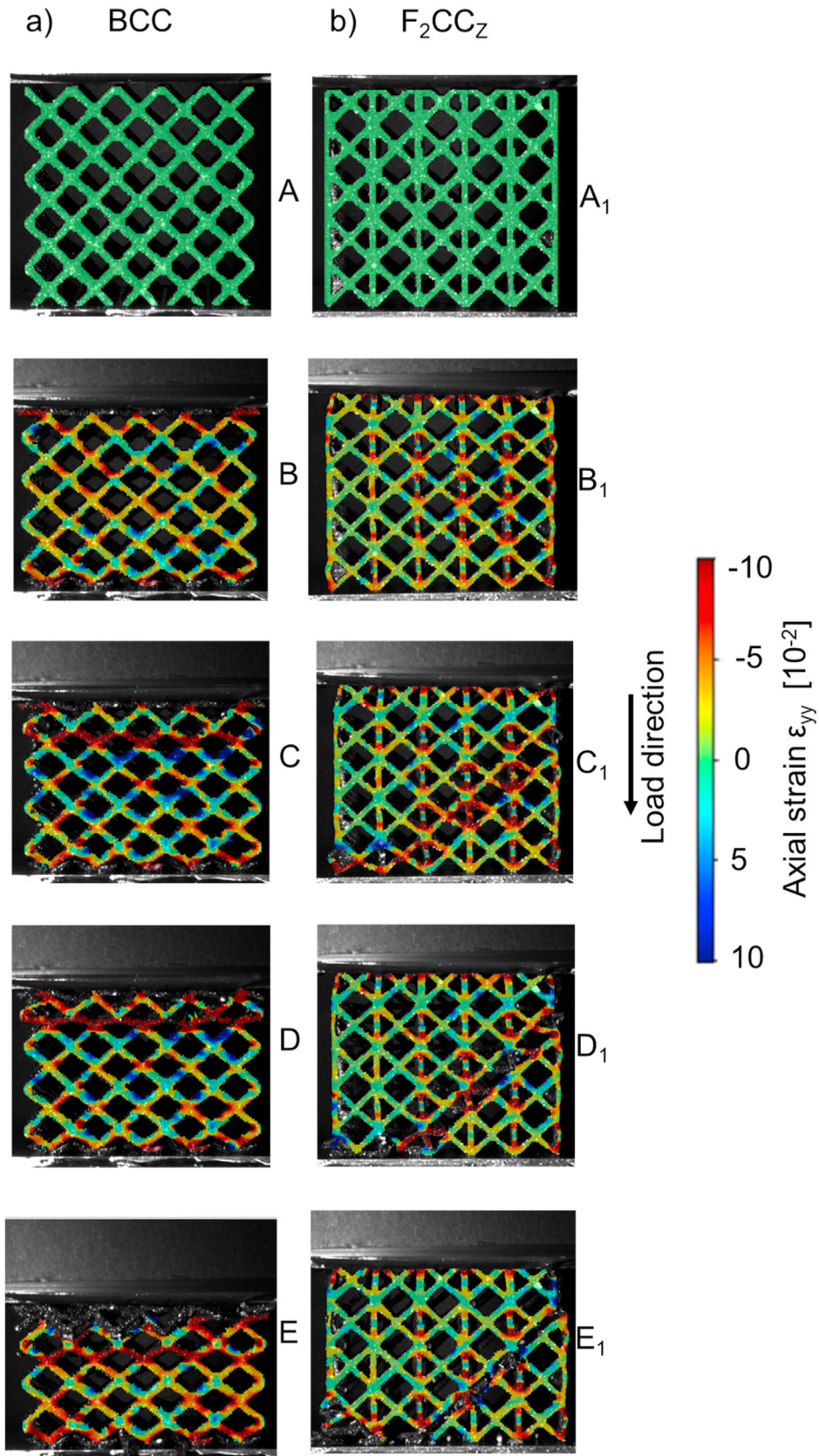
Fig. 12 − DIC images of particular failure pattern during quasi-static compression tests for BCC- and F_2CC_Z-specimens; a) Points A-E (BCC) and b) A1-E1 (F_2CC_Z) correspond to stages highlighted in the stress-compression curves (see Fig. 11).
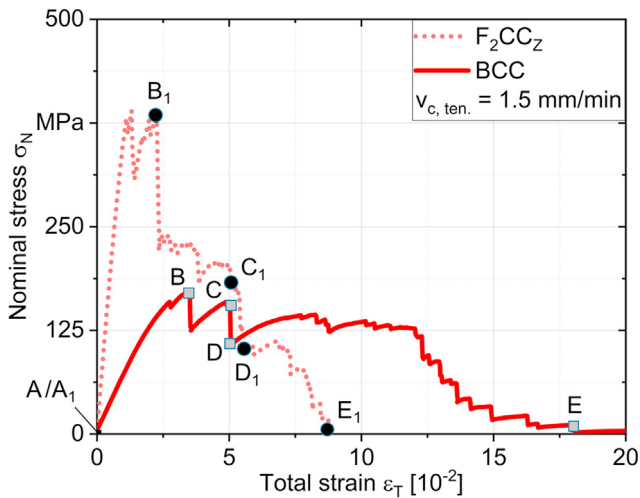
Fig. 13 – **Stress-strain response obtained by quasi-static tensile tests on representative BCC- and F_2CC_Z-specimens. Points labelled by letters refer to the DIC images shown in Fig. 14.**

material behavior is clearly visible. In detail, a five times higher compressive strength could be determined for the stretch-dominated F_2CC_Z-specimen (cf. Fig. 11). However, post yield softening is observed resulting from brittle failure of single struts or unit-cells, which is highlighted by the DIC images in Fig. 12. Comparing the DIC images for both lattice types, different damage mechanisms are visible. For the BCC-specimen failure occurred solely within one lattice plane and is repeated until final densification takes place, whereas failure occurred through several unit-cell planes under a 45° angle within the F_2CC_Z-specimen. This was already reported in Ref. [59]. Kadkhodapur et al. [60] correlated compression curves with failure mechanisms for bending- and stretch-dominated lattice structures and stated that stretch-dominated lattice structures tend to fail layer-by-layer, while bending-dominated structures fail triggered by shear bands. The latter behavior cannot be confirmed in this study, since the bending-dominated lattice structure failed layer-by-layer and the stretch-dominated one failed under a 45° angle. A possible explanation for the deviating deformation behavior, compared to Kadkhodapur et al. [60], might be the varying lattice geometry, which was used for bending- and stretch-dominated deformation behavior. To conclude, stretch-dominated structures are more structurally efficient but are suffered by sudden failure with significant load drops which can be attributed to the brittle material behavior [54]. In comparison, bending-dominated structures are more compliant and show an increased damage tolerance after initial failure.

Comparing the quasi-static behavior under tension, the stress-strain curve is similar to the compression curve in the elastic region, however, after yielding the struts tend to orientate along the loading direction until final failure occurs [54]. As already described, first failure of the F_2CC_Z-specimen occurred at the transition to the bulk material. However, with increasing damage progress the lattice structure failed in a 45°

plane which could not be recorded by the DIC. Future investigations will focus on a modified specimen design with a smooth transition from bulk to the lattice structure. Therefore, different concepts such as graded lattice structures or implementing transition elements will be taken into consideration, as proposed in Refs. [61,62]. In line with the quasi-static compression tests, higher stiffness and yield strength were determined for the F_2CC_Z-specimen, however, a brittle material behavior as well as a smaller degree of plastic deformation were found, which is in line with literature [61,63]. Further on, damage tolerance under tension was found to be lower since the specimen only can bear load on a lower level (63% of peak load) after initial failure compared to the BCC-specimen, which can bear a load of 93% of the initial peak stress after first failure (cf. Fig. 13). Investigations done by Goodall et al. [25] elaborated the effect of simulated processing defects in the form of missing struts. Thereby, it could be shown that the plastic deformation behavior shows a clear trend toward decreasing strength with increasing number of missing struts. This can be directly correlated to the increasing damage progress during quasi-static testing, which might explain the lower stress levels after initial failure for both lattice types. Gibson and Ashby [33] proposed that missing struts can contribute to a change of mode of deformation within porous materials. Considering the DIC images B and C (cf. Fig. 14a) during quasi-static tensile tests, it can clearly be seen that new stress concentrations are forming after initial failure of the BCC-specimen, which can straightforward be attributed to the partial failure before. Classifying the quasi-static properties based on known literature is quiet challenging, since many variables such as manufacturing method, process parameters, lattice morphology and relative density can lead to differing mechanical properties. However, several researchers [16,26] have compared their results to the stiffness of the human bone clearly addressing the reduction of stress shielding effects by reducing the stiffness mismatch between implant and human bone.

Considering literature values [26], the Young's modulus of cancellous and cortical bone is in the range of 0.5–20 GPa. For the F_2CC_Z lattice type, a higher stiffness $E_{F2CCZ} = 34$ GPa could be determined, however, it is significantly lower than for bulk material ($E_{Ti6Al4V} = 118$ GPa [13]). This finally leads to a reduced stiffness mismatch. For the BCC lattice type, a Young's modulus $E_{BCC} = 6.5$ GPa was determined, this being very similar to the human bone. Similar results were earlier reported in Refs. [16,64]. Essential factors, which might influence the stiffness of porous structures, include the pore size or relative density and the morphology of the cell so that stiffness can be adjusted to the individual circumstances by changing these parameters. Nevertheless, the surface topography resulting from the as-built surface roughness can lead to local heterogeneities and the formation of additional stress concentrations, which might affect the initial peak stress during quasi-static testing [26] as well as the material behavior during cyclic loading, which will be discussed later.

3.5. Cyclic properties

Fatigue tests were carried out for both lattice types using a combination of multiple step (MST) and constant amplitude
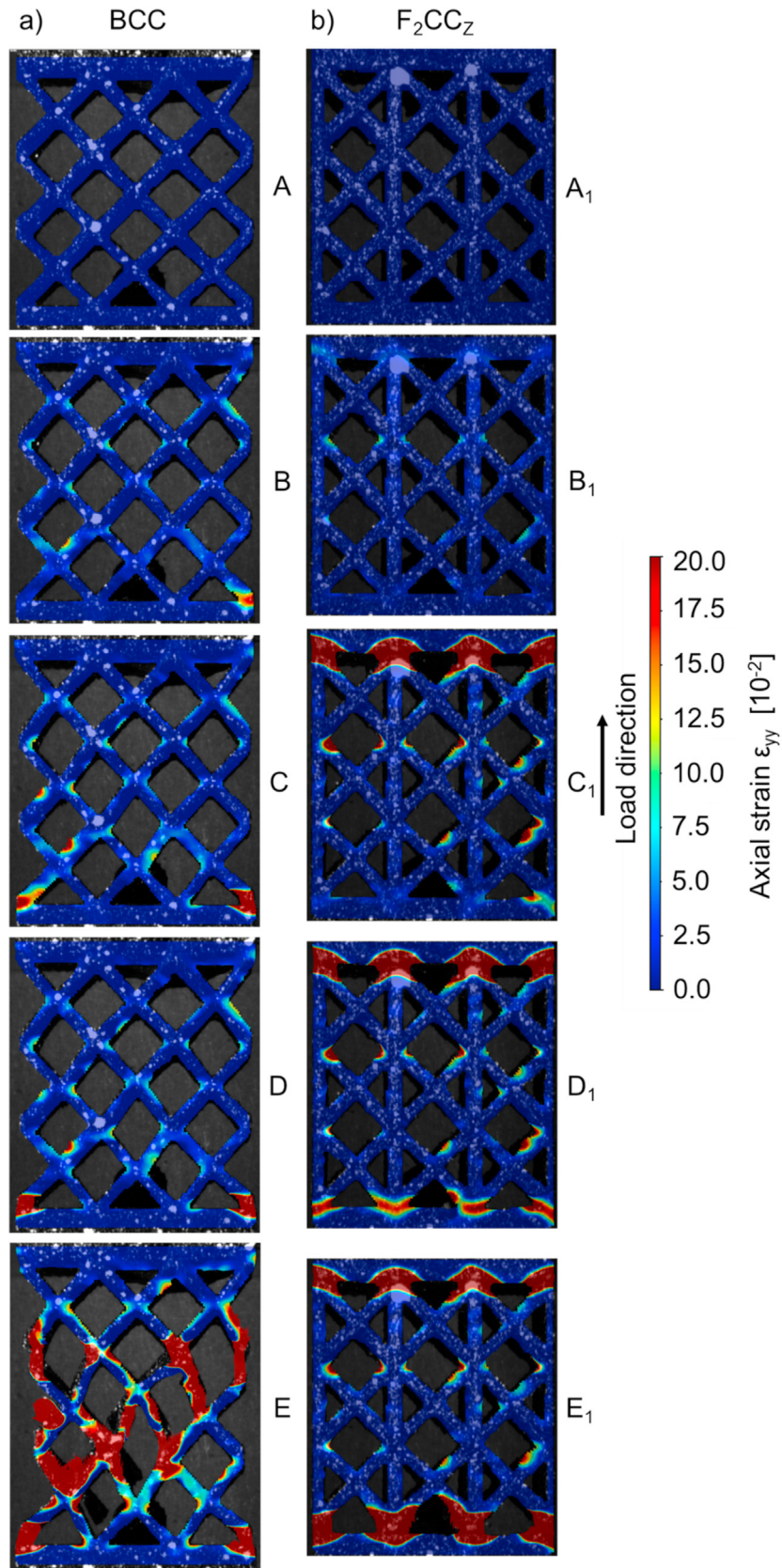
Fig. 14 − **DIC images of particular failure pattern during quasi-static tensile tests for representative BCC- and F$_2$CC$_Z$-specimens; a) A-E and b) A$_1$-E$_1$ correspond to stages highlighted in the stress-strain curves (see Fig. 13).**

tests (CAT). The results of the MST are plotted in Fig. 15. In the diagram, stress amplitudes (σ_a) are colored in blue, changes in electrical resistance (ΔR_{DC}) in orange and the total strain amplitude ($\varepsilon_{a,t}$) in magenta. For the BCC-specimen, a maximum stress amplitude of $\sigma_a = 40$ MPa and a total number of cycles $N_f = 77,323$ cycles were achieved. For comparison, the F_2CC_Z-specimen could reach a maximum stress amplitude of $\sigma_a = 75$ MPa ($N_f = 147,425$ cycles). A first material response in the form of a linear increase in ΔR_{DC} and $\varepsilon_{a,t}$ can be detected for the BCC-specimen at a stress amplitude $\sigma_a = 25$ MPa. With an increasing number of cycles, the linear increase of the measurement quantities changes to an exponential growth ending in final failure. A similar behavior is seen within the results of ΔR_{DC} for the F_2CC_Z-specimen, whereby sudden changes in ΔR_{DC} are additionally present. These features can be attributed to local failure within the lattice structure [36]. Obviously, $\varepsilon_{a,t}$ only shows a slight linear increase followed by an exponential growth shortly before final failure. Based on the results presented, CATs were conducted for both lattice types at stress levels which are in the range of the first material response and the final failure, respectively.

To evaluate the damage progress within the respective lattice structure, similar measurement techniques as for the MST were used for the CATs. In Fig. 16, the material responses for a BCC-specimen tested at a constant stress amplitude of $\sigma_a = 35$ MPa ($N_f = 28,123$ cycles) are highlighted. Analogous to the MST, ΔR_{DC} is colored in orange, $\varepsilon_{a,t}$ in magenta. Additionally, the dynamic Young's modulus E_{dyn} as well as the ratio between dynamic Young's modulus under compression ($E_{dyn,\ comp.}$) and tension ($E_{dyn,\ ten.}$) are plotted versus the number of cycles N. Based on the results depicted, four different stages with specific material responses could be identified, labelled as A-D. The corresponding DIC images are shown Fig. 16a–d. Representative for stage A, the specimen is shown at the beginning of the test in damage-free condition. As can be seen, the course of the measurement quantities is nearly constant until 1.25×10^4 cycles. Thereafter, a linear increase in $\varepsilon_{a,t}$ and ΔR_{DC} can be detected, which can be attributed to the increasing defect density within the lattice structure. At stage B, the first partial failure within the BCC-specimen can be seen based on the DIC images (cf. Fig. 16b). As a consequence, an increase in ΔR_{DC} is visible. Additionally, a stiffness reduction can be detected after the first partial failure, which intensifies with increasing number of cycles until final failure. Resulting from the partial failure within the lattice structure, stress concentrations are formed, which are then the origin of subsequent failure (stages C and D). Both stages are characterized by a sudden increase in ΔR_{DC}, which can be attributed to the decreasing nominal cross section of the lattice structure [36]. The final failure occurred shortly after reaching stage D. The ratio between $E_{dyn,\ comp.}$ and $E_{dyn,\ ten.}$ stays constant over the entire test implicating that no buckling is present, which was earlier reported for two-dimensional (2D) lattice structures [37].

Analogous to the BCC-specimen, the material responses for a F_2CC_Z-specimen tested at a stress amplitude of $\sigma_{a-} = 60$ MPa ($N_f = 108,714$ cycles) are plotted in Fig. 17. Again, measurement quantities ΔR_{DC}, $\varepsilon_{a,t}$, E_{dyn} as well as the ratio $E_{dyn,\ comp.}/E_{dyn,\ ten.}$ were considered. Further on, specific stages (A_1-D_1) within the test are highlighted and the corresponding DIC images are shown in Fig. 17a–d. In Fig. 16a, the specimen is shown at the beginning of the test. The course of ΔR_{DC} and $\varepsilon_{a,t}$ stays stable on the same level until 2.5×10^4 cycles. After reaching stage B_1, a linear increase can be detected for ΔR_{DC} and $\varepsilon_{a,t}$ indicating that the present defect density or rather the effective cross section is negatively influenced by crack initiation and propagation [65]. Even E_{dyn} linearly decreases until stage C_1, where first partial failure can be detected based on the DIC images (cf. Fig. 17c). After the formation of further stress concentration spots and additional partial failure within the lattice structure (stage D_1), an exponential growth can be detected for ΔR_{DC} and $\varepsilon_{a,t}$ as well as an exponential decrease for E_{dyn}.

To provide additional data for the different lattice structures, specimens were investigated by fractographic analysis. The fracture surface of the BCC-specimen ($\sigma_a = 35$ MPa, $N_f = 28,123$ cycles) and the F_2CC_Z-specimen ($\sigma_a = 60$ MPa, $N_f = 108,714$ cycles) is shown in Figs. 18 and 19, respectively. As can be seen, a high number of partially melted powder particles is present on the specimen surfaces and the cross section differs significantly from the ideal round shape, which was already discussed in section 3.3. Nearly all struts failed close to the nodes, i.e., at locations where maximum stresses are presumed. It is obvious, that every specimen contains a high number of fractured surfaces. Most surfaces are characterized by a crack propagation area as well as an overload fracture area, however, the ratio between these areas differ, eventually implying that the size of the crack propagation area is an indicator for the point of failure during the cyclic test. In other words, the bigger the overload fracture area, the later these struts failed. Additionally, small pores and lack of fusion defects are partially visible, however, crack initiation was most often found at the surface.

As already stated, comparing the mechanical properties of lattice structures is quiet challenging since many influencing factors are present. Another concern might be the fact that there are nearly no standards for lattice structures available. Solely ISO 13314 [66] can be considered, introducing a procedure for quasi-static compression testing of metallic porous structures. Eventually, new standards are needed in order to enable a more reproducible determination of mechanical properties in future investigations. However, it is well known that additively manufactured lattice structures are particularly prone to fatigue damage due to various reasons. One key factor is the cell morphology since bulk material is replaced by a unit-cell geometry consisting of several struts, which are connected at different nodes leading to a reduced load bearing area as well as the formation of stress concentrations [54]. Further on, lattice structures are often characterized by geometrical inaccuracies including high surface roughness. These facts provoke differences between the CAD and the as-built parts [48,54]. As mentioned before, the inclination angle of single struts relative to the building direction is also an important factor contributing to a high surface roughness. As a consequence, surface roughness plays a crucial role when considering the fatigue performance, especially for lattice structures, due to the higher surface to volume ratio [49]. Thereby, deep micro-notches are more critical for small-scale structures since they reduce most detrimentally the effective cross section.
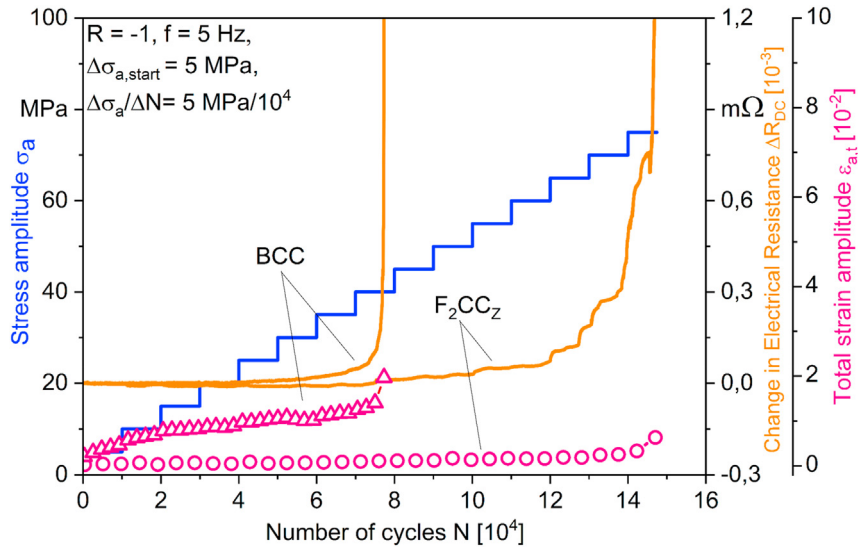
Fig. 15 − Material responses recorded to be used for the analysis of deformation and damage progress in BCC and F$_2$CC$_Z$ lattice structures. Data were obtained in multiple step tests.
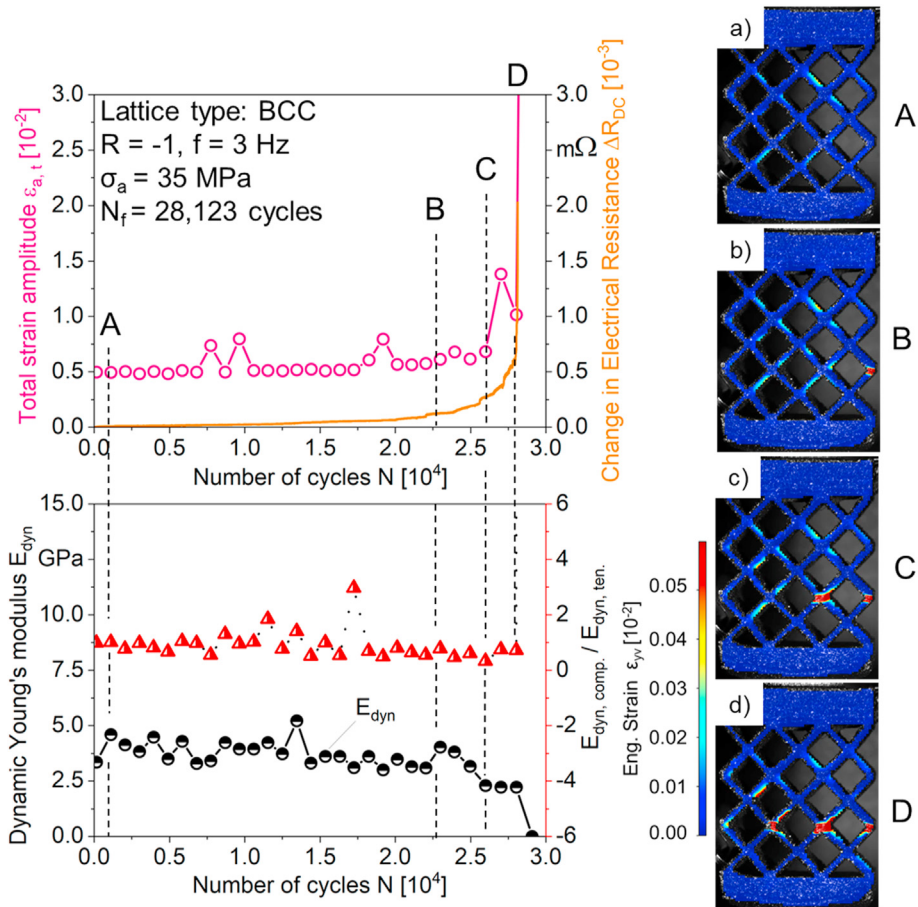

Fig. 16 − Material responses recorded for a BCC lattice structure (σ_a = 35 MPa, N$_f$ = 28,123 cycles) to evaluate the damage progress in constant amplitude tests with corresponding digital image correlation images at specific stages (A−D).
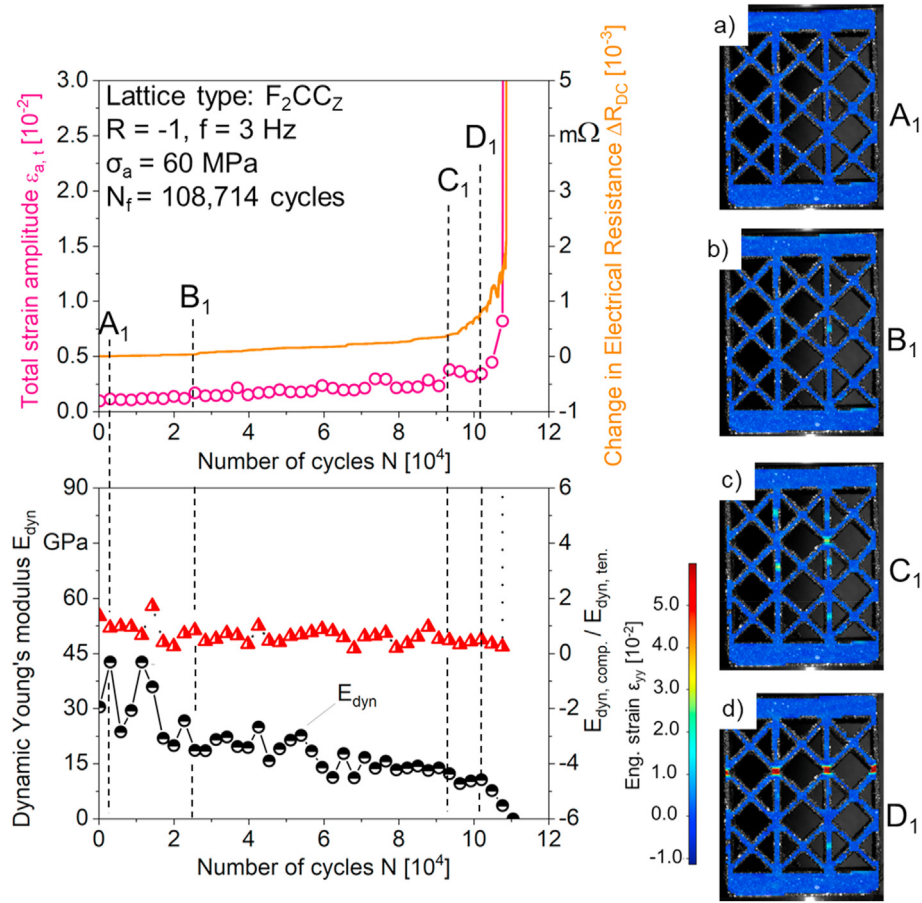
2125

Fig. 17 — Material responses recorded for a F$_2$CC$_Z$ lattice structure (σ_a = 60 MPa, N$_f$ = 108,714 cycles) to evaluate the damage progress in constant amplitude tests with corresponding digital image correlation images at specific stages (A$_1$-D$_1$).
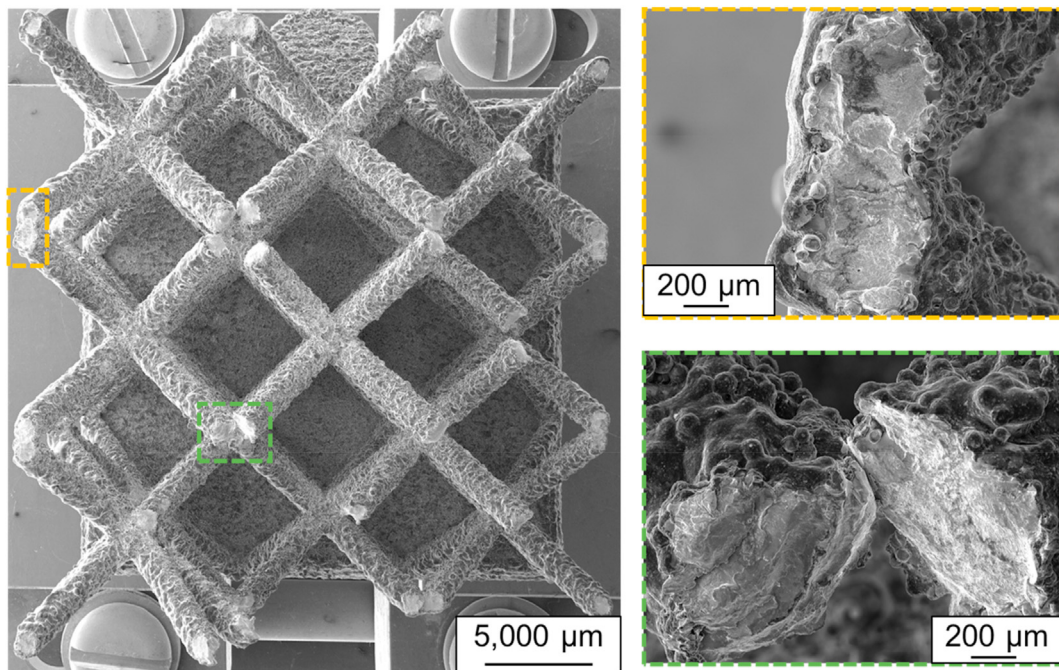

Fig. 18 — Fracture surface of a BCC-specimen tested at a stress amplitude of σ_a = 35 MPa (N$_f$ = 28,123 cycles). The location of the enlarged views is marked by the colored boxes superimposed to the overview image shown to the left.
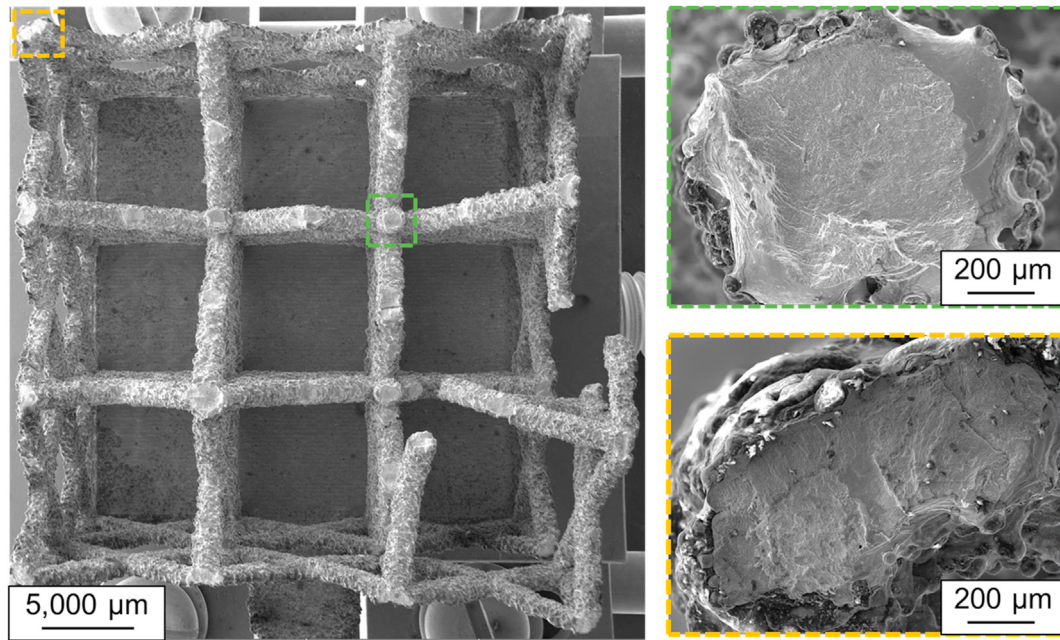
Fig. 19 — Fracture surface of a F_2CC_Z-specimen tested at a stress amplitude of $\sigma_a = 60$ MPa ($N_f = 108,714$ cycles). The location of the enlarged views is marked by the colored boxes superimposed to the overview image shown to the left.

To gain further information about the actual material state during cyclic loading, additional physical measurement methods such as digital image correlation and direct current potential drop system are supplementary used. Typically, material changes can be captured by means of total strain amplitude and assessment of the dynamic Young's modulus. Further on, Piotrowski et al. [65] demonstrated that even resistance measurement techniques can be added to get supplementary data. Thereby, the electrical resistance highly depends on the specific electrical resistance, which is known to be influenced by the actual defect density as well as the effective cross section [67]. Thus, it can be expected that the measurement quantities can be directly correlated with the damage progress. During cyclic testing, lattice structures typically undergo three stages [68]. Within stage I, the structures are dominated by ratcheting, i.e. the progressive accumulation of plastic strain. Stage II is dominated by crack initiation and propagation within the lattice structure and in stage III multiple failure of single struts or nodes is present eventually leading to final failure [54]. Especially stage II and III can reproducibly be captured with the measurement techniques used. In detail, slight increases in ΔR_{DC} and $\varepsilon_{a,t}$ as well as a decrease in E_{dyn} were noticed after a certain number of cycles, which can be directly attributed to fatigue crack initiation and propagation. Furthermore, partial failure of single struts or nodes could be detected through sudden increases in ΔR_{DC} (cf. Figs. 16 and 17) [36]. Especially for the detection of a single strut failure, the use of the DIC system is favored since it enables a better understanding of the occurring damage mechanisms [18,68]. Gorny et al. [17] even used the DIC technique within their investigations clearly highlighting the great potential. With increasing number of cycles, the linear course of the measurement quantities changes to an exponential course due to multiple failure within the lattice structure clearly indicating the beginning of stage III. Failure of single struts mostly occurred close to the nodes where highest tensile stresses appear. As can be seen in the fractographic analysis, inner defects such as gas pores or lack of fusion defects are present on the fracture surface, however, crack initiation sites were located almost exclusively on the specimen surfaces, which is in line with literature [69]. It was stated by Zhao et al. [34] that preferred crack initiation sites were observed around partially melted powder particles on the strut surface, which significantly affects the fatigue performance. Furthermore, multiple crack initiation sites were seen in the fractographic analysis, which is typical for structures which are tested in as-built condition [70]. Coming to crack propagation, failure occurred on a plane perpendicular to the load direction for both lattice types (cf. Figs. 16 and 17). However, it was already proposed in several studies [33,35,71] that different unit-cell types as well as altering relative densities might influence the failure mode. As can be seen, complex geometries, i.e., lattice structures, show a different damage behavior compared to bulk material, which contributes to the growing need for a condition monitoring especially in safety-relevant applications. Additional fatigue tests are needed in order to further investigate the fatigue behavior and to develop a Woehler curve, which can be used as a basis for construction and design processes aiming at the implementation of more AM lattice structures in industrial applications. Further on, new processes have to be established, which can smoothen the surface of lattice structures since the as-built surface roughness was found to be the main reason for early fatigue failure.

4.   Conclusions and outlook

Within this work PBF-EB/M manufactured Ti6Al4V lattice structures were investigated. Thereby, two different structural lattice types, BCC and F_2CC_Z, respectively representatives for bending- and stretch-dominated deformation behavior, were selected. In a primary step, microstructural features were characterized by means of SEM. The results showed nearly identical microstructural features for both lattice types and build heights, which can be rationalized based on the relatively small total lattice height of 21 mm. Thus, it is thought that the microstructure does not affect the mechanical tests. However, the increase of the α-lath width over build height for the BCC lattice, which can be explained by the reduction in heat accumulation over build height, is noticeable from the data and might have an effect on mechanical properties for much higher lattice structures. μCT analysis were conducted to determine the nominal cross section of lattice structures since differences between CAD and as-built parts are present. However, differences in the nominal cross section were found to be similar for each lattice type independent of the number of unit-cells implicating the high reproducibility of the PBF-EB/M process. Within quasi-static compression and tensile tests, the different damage mechanisms for the lattice types could be highlighted, whereby the F_2CC_Z lattice shows a higher overall stiffness and strength, however, it is characterized by a brittle material behavior including significant load drops after first failure. The BCC lattice shows a more ductile material behavior with higher fracture strain and higher load bearing capacity (93% of initial peak stress) after initial failure. During cyclic testing, higher fatigue strength was achieved by the F_2CC_Z lattice structures, however, as-built surface roughness was found to be the main reason for early failure due to multiple crack initiation sites at the specimen surfaces. Furthermore, a direct current potential drop system as well as digital image correlation could be qualified to determine the damage progress during the cyclic tests. In particular, material reactions such as partial failure of single struts or nodes could be correlated with changes in electrical resistance as well as with total strain amplitude and dynamic Young's modulus.

Future investigations will focus on the testing of an increased number of specimens to develop a Woehler curve, which can be used to enhance the number of industrial applications for additively manufactured lattice structures. To further evaluate the cyclic material behavior of additively manufactured lattice structures, different material classes will be processed and tested with the aim to predict the fatigue life as a function of the base material, lattice type, surface condition and relative density.

Declaration of competing interest

The authors declare that they have no known competing financial interests or personal relationships that could have appeared to influence the work reported in this paper.

Acknowledgment

REFERENCES

[1] Herzog D, Seyda V, Wycisk E, Emmelmann C. Additive manufacturing of metals. Acta Mater 2016;117:371–92. https://doi.org/10.1016/j.actamat.2016.07.019.

[2] Körner C. Additive manufacturing of metallic components by selective electron beam melting — a review. Int Mater Rev 2016;61(5):361–77. https://doi.org/10.1080/09506608.2016.1176289.

[3] Liu S, Shin YC. Additive manufacturing of Ti6Al4V alloy: a review, vol. 164. Materials & Design; 2019, 107552. https://doi.org/10.1016/j.matdes.2018.107552.

[4] Murr LE, Gaytan SM, Ramirez DA, Martinez E, Hernandez J, Amato KN, Shindo PW, Medina FR, Wicker RB. Metal fabrication by additive manufacturing using laser and electron beam melting technologies. J Mater Sci Technol 2012;28(1):1–14. https://doi.org/10.1016/S1005-0302(12)60016-4.

[5] Jia Q, Gu D. Selective laser melting additive manufacturing of Inconel 718 superalloy parts: densification, microstructure and properties. J Alloys Compd 2014;585:713–21. https://doi.org/10.1016/j.jallcom.2013.09.171.

[6] Ladani L. Additive manufacturing of metals: materials, processes, tests, and standards. DEStech Publications Inc, Lancaster, Pennsylvania2021.

[7] Kotzem D, Kleszczynski S, Stern F, Elspaß A, Tenkamp J, Witt G, Walther F. Impact of single structural voids on fatigue properties of AISI 316L manufactured by laser powder bed fusion. Int J Fatig 2021;148:106207. https://doi.org/10.1016/j.ijfatigue.2021.106207.

[8] Murr LE, Gaytan SM, Medina F, Lopez H, Martinez E, Machado BI, Hernandez DH, Martinez L, Lopez MI, Wicker RB, Bracke J. Next-generation biomedical implants using additive manufacturing of complex, cellular and functional mesh arrays. Philos Trans A Math Phys Eng Sci 2010;368:1999–2032. https://doi.org/10.1098/rsta.2010.0010. 1917.

[9] Ladani L. Local and global mechanical behavior and microstructure of Ti6Al4V parts built using electron beam melting technology. Metall Mater Trans 2015;46(9):3835–41. https://doi.org/10.1007/s11661-015-2965-6.

[10] Edwards P, O'Conner A, Ramulu M. Electron beam additive manufacturing of titanium components: properties and performance. J Manuf Sci Eng 2013;135(6):525. https://doi.org/10.1115/1.4025773.

[11] Wang P, Sin WJ, Nai MLS, Wei J. Effects of processing parameters on surface roughness of additive manufactured Ti-6Al-4V via electron beam melting. Materials 2017;10(10). https://doi.org/10.3390/ma10101121.

[12] Kotzem D, Höffgen A, Raveendran R, Stern F, Möhring K, Walther F. Position-dependent mechanical characterization of the PBF-EB-manufactured Ti6Al4V alloy. Prog Addit Manuf 2021. https://doi.org/10.1007/s40964-021-00228-9.

[13] Facchini L, Magalini E, Robotti P, Molinari A. Microstructure and mechanical properties of Ti-6Al-4V produced by electron beam melting of pre-alloyed powders. Rapid Prototyp J 2009;15(3):171—8. https://doi.org/10.1108/13552540910960262.

[14] Ridzwan M, Shuib S, Hassan AY, Shokri AA, Mohamad Ib MN. Problem of stress shielding and improvement to the hip implant designs: a review. J Med Sci 2007;7(3):460—7. https://doi.org/10.3923/jms.2007.460.467.

[15] Cheng XY, Li SJ, Murr LE, Zhang ZB, Hao YL, Yang R, Medina F, Wicker RB. Compression deformation behavior of Ti-6Al-4V alloy with cellular structures fabricated by electron beam melting. J Mech Behav Biomed Mater 2012;16:153—62. https://doi.org/10.1016/j.jmbbm.2012.10.005.

[16] Heinl P, Müller L, Körner C, Singer RF, Müller FA. Cellular Ti-6Al-4V structures with interconnected macro porosity for bone implants fabricated by selective electron beam melting. Acta Biomater 2008;4(5):1536—44. https://doi.org/10.1016/j.actbio.2008.03.013.

[17] Gorny B, Niendorf T, Lackmann J, Thoene M, Troester T, Maier HJ. In situ characterization of the deformation and failure behavior of non-stochastic porous structures processed by selective laser melting. Mater Sci Eng, A 2011;528(27):7962—7. https://doi.org/10.1016/j.msea.2011.07.026.

[18] Brenne F, Niendorf T, Maier HJ. Additively manufactured cellular structures: impact of microstructure and local strains on the monotonic and cyclic behavior under uniaxial and bending load. J Mater Process Technol 2013;213(9):1558—64. https://doi.org/10.1016/j.jmatprotec.2013.03.013.

[19] Brenne F, Niendorf T. Load distribution and damage evolution in bending and stretch dominated Ti-6Al-4V cellular structures processed by selective laser melting. Int J Fatig 2019;121:219—28. https://doi.org/10.1016/j.ijfatigue.2018.12.017.

[20] Cansizoglu O, Harrysson O, Cormier D, West H, Mahale T. Properties of Ti—6Al—4V non-stochastic lattice structures fabricated via electron beam melting. Mater Sci Eng, A 2008;492(1—2):468—74. https://doi.org/10.1016/j.msea.2008.04.002.

[21] Ashby MF. The properties of foams and lattices. Philos Trans A Math Phys Eng Sci 2006;364:15—30. https://doi.org/10.1098/rsta.2005.1678. 1838.

[22] Maxwell JCL. On the calculation of the equilibrium and stiffness of frames. The London, Edinburgh, and Dublin Philosophical Magazine and Journal of Science 1864;27(182):294—9. https://doi.org/10.1080/14786446408643668.

[23] Yan C, Hao L, Hussein A, Young P. Ti-6Al-4V triply periodic minimal surface structures for bone implants fabricated via selective laser melting. J Mech Behav Biomed Mater 2015;51:61—73. https://doi.org/10.1016/j.jmbbm.2015.06.024.

[24] Aşık EE, Bor Ş. Fatigue behavior of Ti—6Al—4V foams processed by magnesium space holder technique. Mater Sci Eng, A 2015;621:157—65. https://doi.org/10.1016/j.msea.2014.10.068.

[25] Goodall R, Hernandez-Nava E, Jenkins SNM, Sinclair L, Tyrwhitt-Jones E, Khodadadi MA, Ip DH, Ghadbeigi H. The effects of defects and damage in the mechanical behavior of Ti6Al4V lattices. Front. Mater. 2019;6:66. https://doi.org/10.3389/fmats.2019.00117.

[26] Parthasarathy J, Starly B, Raman S, Christensen A. Mechanical evaluation of porous titanium (Ti6Al4V) structures with electron beam melting (EBM). J Mech Behav Biomed Mater 2010;3(3):249—59. https://doi.org/10.1016/j.jmbbm.2009.10.006.

[27] Epasto G, Palomba G, D'Andrea D, Guglielmino E, Di Bella S, Traina F. Ti-6Al-4V ELI microlattice structures manufactured by electron beam melting: effect of unit cell dimensions and morphology on mechanical behaviour. Mater Sci Eng, A 2019;753:31—41. https://doi.org/10.1016/j.msea.2019.03.014.

[28] Ataee A, Li Y, Fraser D, Song G, Wen C. Anisotropic Ti-6Al-4V gyroid scaffolds manufactured by electron beam melting (EBM) for bone implant applications. Mater Des 2018;137:345—54. https://doi.org/10.1016/j.matdes.2017.10.040.

[29] Hernández-Nava E, Smith CJ, Derguti F, Tammas-Williams S, Leonard F, Withers PJ, Todd I, Goodall R. The effect of defects on the mechanical response of Ti-6Al-4V cubic lattice structures fabricated by electron beam melting. Acta Mater 2016;108:279—92. https://doi.org/10.1016/j.actamat.2016.02.029.

[30] Galati M, Saboori A, Biamino S, Calignano F, Lombardi M, Marchiandi G, Minetola P, Fino P, Iuliano L. Ti-6Al-4V lattice structures produced by EBM: heat treatment and mechanical properties. Procedia CIRP 2020;88:411—6. https://doi.org/10.1016/j.procir.2020.05.071.

[31] Formanoir C de, Suard M, Dendievel R, Martin G, Godet S. Improving the mechanical efficiency of electron beam melted titanium lattice structures by chemical etching. Addit Manuf 2016;11:71—6. https://doi.org/10.1016/j.addma.2016.05.001.

[32] Li SJ, Murr LE, Cheng XY, Zhang ZB, Hao YL, Yang R, Medina F, Wicker RB. Compression fatigue behavior of Ti—6Al—4V mesh arrays fabricated by electron beam melting. Acta Mater 2012;60(3):793—802. https://doi.org/10.1016/j.actamat.2011.10.051.

[33] Gibson LJ, Ashby MF. Cellular solids. Cambridge University Press2014.

[34] Zhao S, Li SJ, Hou WT, Hao YL, Yang R, Misra RDK. The influence of cell morphology on the compressive fatigue behavior of Ti-6Al-4V meshes fabricated by electron beam melting. J Mech Behav Biomed Mater 2016;59:251—64. https://doi.org/10.1016/j.jmbbm.2016.01.034.

[35] Lietaert K, Cutolo A, Boey D, van Hooreweder B. Fatigue life of additively manufactured Ti6Al4V scaffolds under tension-tension, tension-compression and compression-compression fatigue load. Sci Rep 2018;8(1):4957. https://doi.org/10.1038/s41598-018-23414-2.

[36] Kotzem D, Arold T, Niendorf T, Walther F. Damage tolerance evaluation of E-PBF-manufactured Inconel 718 strut geometries by advanced characterization techniques. Materials 2020;13(1):1—21. https://doi.org/10.3390/ma13010247.

[37] Kotzem D, Ohlmeyer H, Walther F. Damage tolerance evaluation of a unit cell plane based on electron beam powder bed fusion (E-PBF) manufactured Ti6Al4V alloy. Procedia Struct Integr 2020;28:11—8. https://doi.org/10.1016/j.prostr.2020.10.003.

[38] Ran J, Jiang F, Sun X, Chen Z, Tian C, Zhao H. Microstructure and mechanical properties of Ti-6Al-4V fabricated by electron beam melting. Crystals 2020;10(11):972. https://doi.org/10.3390/cryst10110972.

[39] Alaghmandfard R, Dharmendra C, Odeshi AG, Mohammadi M. Dynamic mechanical properties and failure characteristics of electron beam melted Ti-6Al-4V under high strain rate impact loadings. Mater Sci Eng, A 2020;793:139794. https://doi.org/10.1016/j.msea.2020.139794.

[40] Kenel C, Grolimund D, Li X, Panepucci E, Samson VA, Sanchez DF, Marone F, Leinenbach C. In situ investigation of phase transformations in Ti-6Al-4V under additive manufacturing conditions combining laser melting and

high-speed micro-X-ray diffraction. Sci Rep 2017;7(1):16358. https://doi.org/10.1038/s41598-017-16760-0.

[41] Downing D, Leary M, McMillan M, Alghamdi A, Brandt M. Heat transfer in lattice structures during metal additive manufacturing: numerical exploration of temperature field evolution. Rapid Prototyp J 2020;26(5):911—28. https://doi.org/10.1108/RPJ-11-2018-0288.

[42] Zhao H, Ho A, Davis A, Antonysamy A, Prangnell P. Automated image mapping and quantification of microstructure heterogeneity in additive manufactured Ti6Al4V. Mater Char 2019;147:131—45. https://doi.org/10.1016/j.matchar.2018.10.027.

[43] Al-Bermani SS, Blackmore ML, Zhang W, Todd I. The origin of microstructural diversity, texture, and mechanical properties in electron beam melted Ti-6Al-4V. Metall Mater Trans 2010;41(13):3422—34. https://doi.org/10.1007/s11661-010-0397-x.

[44] Chang K, Wang X, Liang E, Zhang R. On the texture and mechanical property anisotropy of Ti6Al4V alloy fabricated by powder-bed based laser additive manufacturing. Vacuum 2020;181:109732. https://doi.org/10.1016/j.vacuum.2020.109732.

[45] Syed AK, Parfitt D, Wimpenny D, Muzangaza E, Chen B. Cyclic plasticity and damage mechanisms of Ti-6Al-4V processed by electron beam melting. Int J Fatig 2022;160:106883. https://doi.org/10.1016/j.ijfatigue.2022.106883.

[46] Yan C, Hao L, Hussein A, Young P, Raymont D. Advanced lightweight 316L stainless steel cellular lattice structures fabricated via selective laser melting. Mater Des 2014;55:533—41. https://doi.org/10.1016/j.matdes.2013.10.027.

[47] Arabnejad S, Burnett Johnston R, Pura JA, Singh B, Tanzer M, Pasini D. High-strength porous biomaterials for bone replacement: a strategy to assess the interplay between cell morphology, mechanical properties, bone ingrowth and manufacturing constraints. Acta Biomater 2016;30:345—56. https://doi.org/10.1016/j.actbio.2015.10.048.

[48] Suard M, Martin G, Lhuissier P, Dendievel R, Vignat F, Blandin J-J, Villeneuve F. Mechanical equivalent diameter of single struts for the stiffness prediction of lattice structures produced by Electron Beam Melting. Addit Manuf 2015;8:124—31. https://doi.org/10.1016/j.addma.2015.10.002.

[49] Razavi S, van Hooreweder B, Berto F. Effect of build thickness and geometry on quasi-static and fatigue behavior of Ti-6Al-4V produced by Electron Beam Melting. Addit Manuf 2020;36:101426. https://doi.org/10.1016/j.addma.2020.101426.

[50] Sombatmai A, Uthaisangsuk V, Wongwises S, Promoppatum P. Multiscale investigation of the influence of geometrical imperfections, porosity, and size-dependent features on mechanical behavior of additively manufactured Ti-6Al-4V lattice struts. Mater Des 2021;209:109985. https://doi.org/10.1016/j.matdes.2021.109985.

[51] Chahid Y, Racasan R, Pagani L, Townsend A, Liu A, Bills P, Blunt L. Parametrically designed surface topography on CAD models of additively manufactured lattice structures for improved design validation. Addit Manuf 2021;37:101731. https://doi.org/10.1016/j.addma.2020.101731.

[52] DIN Deutsches Institut für Normung e.V. Prüfung metallischer Werkstoffe — druckversuch bei Raumtemperatur. 2016, 50106. [Accessed 18 March 2020].

[53] Del Guercio G, Galati M, Saboori A. Innovative approach to evaluate the mechanical performance of Ti—6Al—4V lattice structures produced by electron beam melting process. Met Mater Int 2021;27(1):55—67. https://doi.org/10.1007/s12540-020-00745-2.

[54] Benedetti M, Du Plessis A, Ritchie RO, Dallago M, Razavi S, Berto F. Architected cellular materials: a review on their mechanical properties towards fatigue-tolerant design and fabrication. Mater Sci Eng R Rep 2021;144:100606. https://doi.org/10.1016/j.mser.2021.100606.

[55] Nazir A, Abate KM, Kumar A, Jeng J-Y. A state-of-the-art review on types, design, optimization, and additive manufacturing of cellular structures. Int J Adv Manuf Technol 2019;104(9—12):3489—510. https://doi.org/10.1007/s00170-019-04085-3.

[56] Zhong T, He K, Li H, Yang L. Mechanical properties of lightweight 316L stainless steel lattice structures fabricated by selective laser melting. Mater Des 2019;181:108076. https://doi.org/10.1016/j.matdes.2019.108076.

[57] Leary M, Mazur M, Elambasseril J, McMillan M, Chirent T, Sun Y, Qian M, Easton M, Brandt M. Selective laser melting (SLM) of AlSi12Mg lattice structures. Mater Des 2016;98:344—57. https://doi.org/10.1016/j.matdes.2016.02.127.

[58] Mohammadhosseini A, Masood SH, Fraser D, Jahedi M, Gulizia S. Flexural behaviour of titanium cellular structures produced by electron beam melting. Mater Today Proc 2017;4(8):8260—8. https://doi.org/10.1016/j.matpr.2017.07.168.

[59] Leary M. Design of titanium implants for additive manufacturing. In: Froes FH, Qian M (eds) Titanium in medical and dental applications. Woodhead Publishing an imprint of Elsevier, Duxford, United Kingdom2018), 203—224.

[60] Kadkhodapour J, Montazerian H, Darabi AC, Anaraki AP, Ahmadi SM, Zadpoor AA, Schmauder S. Failure mechanisms of additively manufactured porous biomaterials: effects of porosity and type of unit cell. J Mech Behav Biomed Mater 2015;50:180—91. https://doi.org/10.1016/j.jmbbm.2015.06.012.

[61] Merkt S. Qualifizierung von generativ gefertigten Gitterstrukturen für maßgeschneiderte Bauteilfunktionen. Dissertation, RWTH Aachen. 2015.

[62] Drücker S, Lüdeker JK, Blecken M, Kurt A, Betz K, Kriegesmann B, Fiedler B. Probabilistic analysis of additively manufactured polymer lattice structures. Mater Des 2022;213:110300. https://doi.org/10.1016/j.matdes.2021.110300.

[63] Köhnen P, Haase C, Bültmann J, Ziegler S, Schleifenbaum JH, Bleck W. Mechanical properties and deformation behavior of additively manufactured lattice structures of stainless steel. Mater Des 2018;145:205—17. https://doi.org/10.1016/j.matdes.2018.02.062.

[64] Gatto ML, Groppo R, Bloise N, Fassina L, Visai L, Galati M, Iuliano L, Mengucci P. Topological, mechanical and biological properties of Ti6Al4V scaffolds for bone tissue regeneration fabricated with reused powders via electron beam melting. Materials 2021;14(1). https://doi.org/10.3390/ma14010224.

[65] Piotrowski A, Eifler D. Bewertung zyklischer Verformungsvorgänge metallischer Werkstoffe mit Hilfe mechanischer, thermometrischer und elektrischer meßverfahren Characterization of cyclic deformation behaviour by mechanical, thermometrical and electrical methods. Mat.-wiss. u. Werkstofftech. 1995;26:121—7.

[66] International Organization for Standardization. Mechanical testing of metals - ductility testing - compression test for porous and cellular metals. 2011, 13314. [Accessed 19 March 2020].

[67] Walther F, Eifler D. Cyclic deformation behavior of steels and light-metal alloys. Mater Sci Eng, A 2007:468—70. https://doi.org/10.1016/j.msea.2006.06.146. 259—266.

[68] Yavari SA, Wauthle R, van der Stok J, Riemslag AC, Janssen M, Mulier M, Kruth JP, Schrooten J, Weinans H, Zadpoor AA. Fatigue behavior of porous biomaterials manufactured using selective laser melting. Mater Sci Eng C Mater Biol Appl 2013;33(8):4849—58. https://doi.org/10.1016/j.msec.2013.08.006.

[69] Dallago M, Fontanari V, Torresani E, Leoni M, Pederzolli C, Potrich C, Benedetti M. Fatigue and biological properties of

Ti-6Al-4V ELI cellular structures with variously arranged cubic cells made by selective laser melting. J Mech Behav Biomed Mater 2018;78:381—94. https://doi.org/10.1016/j.jmbbm.2017.11.044.

[70] Kahlin M, Ansell H, Moverare JJ. Fatigue behaviour of additive manufactured Ti6Al4V, with as-built surfaces, exposed to variable amplitude loading. Int J Fatig 2017;103:353—62. https://doi.org/10.1016/j.ijfatigue.2017.06.023.

[71] Kotzem D, Tazerout D, Arold T, Niendorf T, Walther F. Failure mode map for E-PBF manufactured Ti6Al4V sandwich panels. Eng Fail Anal 2021;121:105159. https://doi.org/10.1016/j.engfailanal.2020.105159.